LASER & PHOTONICS REVIEWS

www.lpr-journal.org

Chiral Bound States in the Continuum in Plasmonic Metasurfaces

Yuhu Tang, Yao Liang, Jin Yao, Mu Ku Chen, Shirong Lin, Zhuo Wang, Jingcheng Zhang, Xu Guang Huang,* Changyuan Yu,* and Din Ping Tsai**

Bound states in the continuum (BICs) offer novel mechanisms to boost the quality factor (Q-factor) of resonances. Unfortunately, current studies on chiral BICs metasurfaces suffer from a fundamental trade-off between Q-factor and circular dichroism (CD), presenting a significant hurdle that severely limits the independent control between CD and Q-factors. Here, 3D plasmonic metasurfaces are numerically demonstrated that overcome the trade-off and offer high-Q quasi-BIC resonances (Q ≈ 938) with strong CD (≈0.67) in the mid-infrared. These metasurfaces are made of integrated-resonance units consisting of a twisted vertical split-ring resonator (VSRR) and a wall. Importantly, this dissimilar dimer configuration unlocks a new degree of freedom to decouple the Q-factor and CD, that is, the Q-factor and CD can be relatively independently manipulated by the height of the wall and the twisted angle of the VSRR, respectively. These results provide novel paradigms to manipulate advanced chiroptical responses, with various applications that require strong CD with enhanced light–matter interaction.

1. Introduction

Photonic bound states in the continuum (BICs) describe exotic localized eigenstates embedded in the continuum spectrum. Since its initial mathematical prediction in quantum mechanics,[1] the concept of BICs has been explored in both quantum and classical regimes.[2,3] In theory, BICs physics allows for resonances with infinite quality factor (*Q*-factor) in both individual particles and arrays due to its elimination of radiation loss.[4,5] In practice, BICs often turn into quasi-BICs with finite yet high *Q*-factor due to practical imperfections in fabrication, characterization, finite-size effects, and other factors. In particular, high *Q*-factor resonances driven by quasi-BICs represent a novel scheme for spectrum linewidth engineering,[6] which has enabled many promising applications that required strong light–matter interaction, such as Bose–Einstein condensation,[7,8] lasing,[9,10] biosensing,[11] nonlinear harmonic generation,[12,13] and many others.

Chiral plasmonic nanostructures have gained extensive interest for their capacity in advanced light spin manipulation.[14,15] To date, many schemes have been proposed to construct chiral plasmonics, such as gold helix,[16] multilayer twisted configurations,[17,18] near-field coupling dimers,[19–21] DNA origami,[22,23] folded metasurfaces empowered by Nanokirigami,[24,25] superlattice far-field interference,[26,27] and extrinsic optical chirality in achiral metasurfaces.[28,29] However, the above-mentioned schemes suffer from a common disadvantage of low *Q*-factor resonances (often $Q \approx 10$) due to intrinsic plasmonic damping and radiation loss. This inevitably hinders their potential applications in the fields requiring sharp resonance with strong field enhancement. For example, chiral lasing[30] and quantum entanglement.[31,32]

To address this challenge, the idea of combining high-*Q* quasi-BICs resonances with chirality seems promising. To this end, several pioneering studies reported on the creation of chiral quasi-BIC resonances with giant circular dichroism (CD) in dielectric platforms. These include pairs of ellipse dimers with a small out-of-plane distance,[33] tilted etch twisted dimers,[34] asymmetric high aspect ratio silicon disk arrays,[35] and bilayer twisted dimers metasurfaces.[36,37] Similar mechanisms were employed to create chiral BICs in plasmonic platforms supporting surface lattice

Y. Tang, X. G. Huang
Guangdong Provincial Key Laboratory of Nanophotonic Functional Materials and Devices and Guangzhou Key Laboratory for Special Fiber Photonic Devices and Applications
South China Normal University
Guangzhou 510006, P. R. China
E-mail: huangxg@scnu.edu.cn

Y. Tang, Z. Wang, C. Yu
Photonics Research Institute
Department of Electronic and Information Engineering
The Hong Kong Polytechnic University
Kowloon, Hong Kong 999077, P. R. China
E-mail: changyuan.yu@polyu.edu.hk

Y. Liang, J. Yao, M. K. Chen, J. Zhang, D. P. Tsai
The State Key Laboratory of Terahertz and Millimeter Waves
Centre for Biosystems, Neuroscience and Nanotechnology
City University of Hong Kong
Kowloon, Hong Kong 999077, P. R. China
E-mail: yaoliang@m.scnu.edu.cn; dptsai@cityu.edu.hk

S. Lin
School of Physical Sciences
Great Bay University
Dongguan, Guangdong Province 523000, P. R. China

The ORCID identification number(s) for the author(s) of this article can be found under https://doi.org/10.1002/lpor.202200597

DOI: 10.1002/lpor.202200597

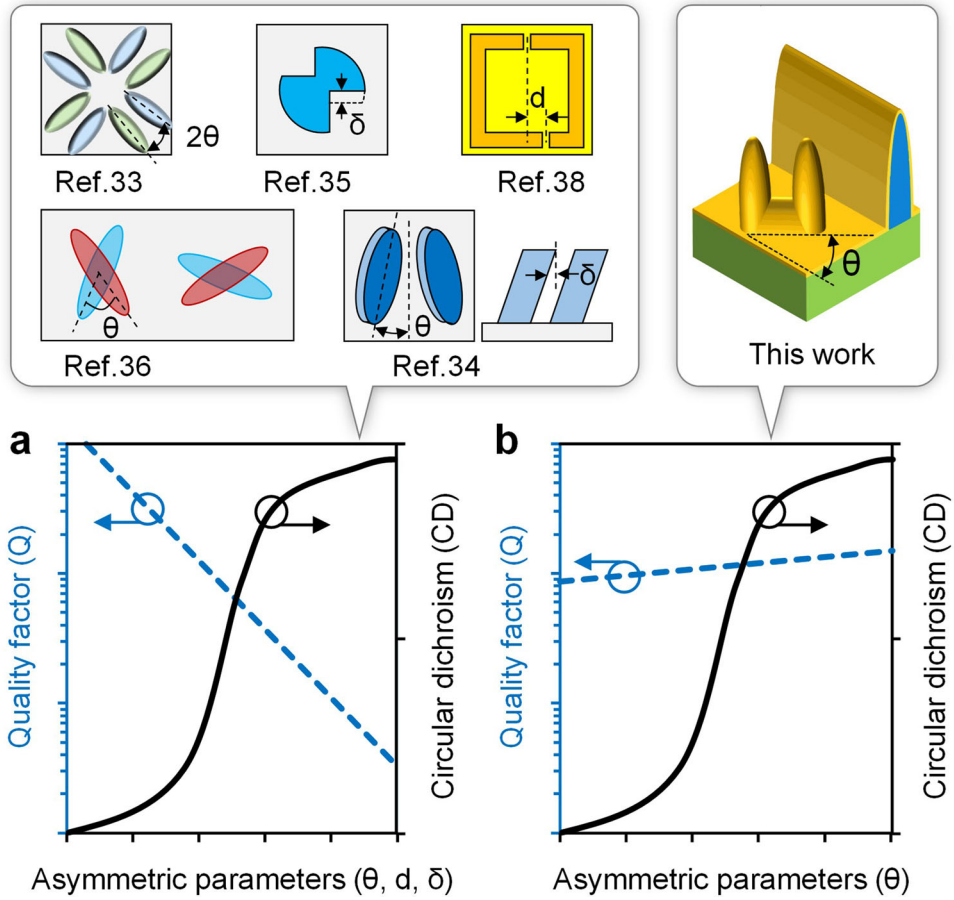

Figure 1. a) Schematics of the dependence of *Q*-factor and circular dichroism (CD) on the asymmetric parameters for chiral quasi-BIC resonances reported by previous studies.[33–36,38] The inserted images show the corresponding metasurface configurations. b) The counterparts in this work.

resonances (SLRs).[38–40] One representative example is based on a pair of gold split-ring resonators (SRRs) on a gold mirror.[38] This configuration allows for spin-selective absorption due to the excitation of chiral quasi-BIC resonances. However, the above-highlighted examples face a fundamental trade-off between the *Q*-factor and CD. This is related to their configurations, where the CD and *Q*-factor of the chiral quasi-BIC resonances are strongly correlated.[33,36,38] In other words, an increase in the asymmetric parameters (twisted angles or/and geometric dimensions) on the one hand leads to an increase in the CD but on the other hand an exponential increase in the radiation loss.[33,36,38] Consequently, the radiation *Q*-factor of chiral quasi-BIC resonance decreases several orders of magnitude before the CD reaches maximum,[38] as shown in **Figure 1**a. This poses a fundamental challenge for the realization of plasmonic quasi-BIC resonances in meta-devices with independent control on the *Q*-factor and CD simultaneously.

In this work, for the first time to the best of our knowledge, we address this challenge by designing novel chiral BIC metasurfaces with integrated-resonance units (IRUs)[41] supporting quasi-BICs resonances with both high-*Q* and strong CD in mid-infrared regimes. Specifically, our metasurfaces consist of a 2D twisted vertical split-ring resonators (VSRRs) array and a 1D grating (wall). This dissimilar configuration is deliberately chosen for its unique properties. For example, it allows for the decoupling between CD and *Q*-factor so that the *Q*-factor is primarily determined by the wall while the CD is related to the twisted angle of VSRRs. In sharp contrast to previous demonstrations, where the *Q*-factor of quasi-BIC resonances decreases as the CD increases, in our metasurfaces, the *Q*-factor remains stable as one twists the VSRR to obtain different values of CD, as shown in Figure 1b. Our results unlock a new degree of freedom for CD manipulation in high-*Q* plasmonic quasi-BIC resonances with promising potential applications ranging from chiral molecule detection to quantum information processing.

2. Integrated-Resonance Unit and BICs

Unlike most previous studies of chiral BICs, which are mostly based on dimer configuration with two subunits of similar size and shape,[33,36,38] the integrated-resonance unit of our metasurface consists of two dissimilar subunits, which are a twisted vertical split-ring resonator (VSRRs) and a wall (**Figure 2**a). The geometric details of an IRU are shown in Figure 2b,c. This configuration lacks mirror symmetry and is expected to show optical chirality.

Our metasurfaces can be fabricated using standard and mature techniques, which are, two-photon polymerization gold

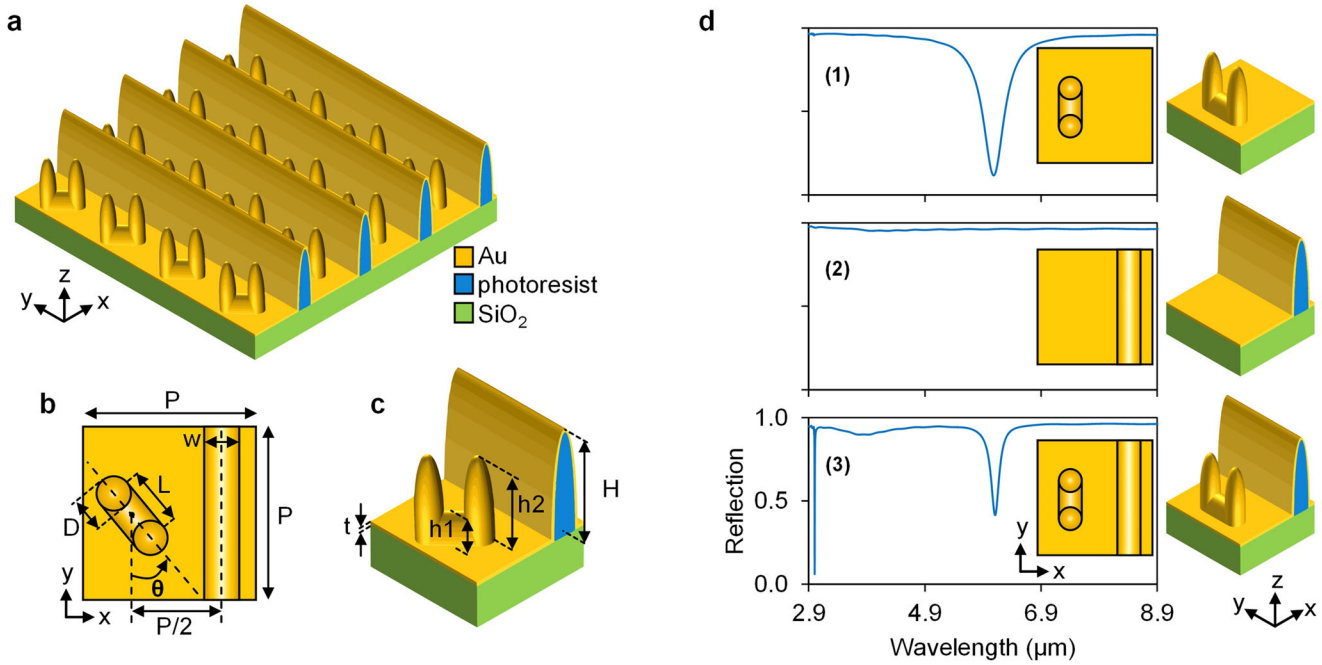

Figure 2. a) Schematic showing an array of the proposed metasurfaces. b) Top view of one unit. c) Side view of one unit. The geometric parameters are $P = 3$ μm, $D = 0.6$ μm, $t = 0.1$ μm, $h1 = 0.6$ μm, $h2 = 1.8$ μm, $w = 0.6$ μm, $H = 2.4$ μm, and $\theta = 35°$. d) Reflection spectra for three metasurfaces consisting of (1) one VSRR unit; (2) a single wall unit; (3) an integrated-resonance unit (diatomic) under *y*-polarized light illumination at normal incidence.

sputtering.[42] To make it fabrication-friendly, curved wall tops and semi-ellipsoid pillar tops are deliberately designed such that they can be easily fabricated by standard laser writing.[43] The lattice period of our metasurfaces is $P = 3$ μm and we choose 100 nm gold film for our metasurfaces to prevent transmission (T) in the mid-infrared range, and thus the absorption (A) can be calculated as $A = 1-R$, where R is the reflection.

One reason why we choose two dissimilar subunits is to create sharp quasi-BIC resonances. To illustrate this, we perform full-wave simulations to study the metasurfaces using COMSOL Multiphysics (see Experimental Section for details). Figure 2d displays the reflection spectra for three anisotropic metasurfaces under normal incident light illumination (y-polarized), whose eigenmodes are polarization independent due to the in-plane inversion (C_2) symmetry.[44] Interestingly, in sharp contrast to single meta-atom metasurfaces consisting of either a VSRR or a wall, the diatomic IRU shows a sharp ($Q \approx 715$) surface lattice resonance (SLR) at $\lambda = 3.0026$ μm. Here the Q-factor is defined as the ratio between the resonance wavelength and the full width at half maximum. This SLR mode can only be supported in the IRU metasurface, which has its roots in BICs in the parameter space.

To illustrate this, we change the height (H) of the wall subunit from 0 to 5.2 μm, and the evolution of the reflection spectra of the SLR is shown in **Figure 3**a. As H increases, the SLR mode gradually appears with the spectral linewidth and resonance depth increasing simultaneously. After passing its resonance depth peak value at $H = 2.4$ μm, the SLR gradually disappears with narrowing spectral linewidth (increasing Q-factor) as H increases further. This is a transition process from BIC to quasi-BICs and back to BIC, revealing the BIC origin of the high Q-factor SLRs in the parameter space. In our plasmonic systems, the BICs have finite Q-factors due to the dissipation loss of gold.

In particular, during the transition between BICs and quasi-BICs, there is a resonance energy shift between two subunits. The gold material in our metasurfaces can generate dissipation loss at resonances. The dissipation power density (W m^{-3}) of the metasurfaces can be expressed as[45]

$$w\ (r) = \frac{1}{2}\ \varepsilon_0 \omega \mathrm{Im}\left[\varepsilon\ (r)\right] E\,(r) \cdot E(r)^* \tag{1}$$

where ε_0 is the vacuum permittivity, $\varepsilon(r)$ the material permittivity at various positions $r(x, y, z)$, and $E(r)$ the electric field. Since our metasurfaces do not contain magnetic materials, magnetic loss is not included. The dissipation power density (at quasi-BICs resonance) for various metasurfaces (different H) is shown in Figure 3b (top panel). As the BICs transit into quasi-BICs, the dissipation power density gradually shifts from the VSRR to the wall. To quantitatively describe this resonance energy shifting between two subunits, we calculate the absorption of each subunit in various quasi-BICs using

$$A_i = \frac{\iiint w\,(r)\,\mathrm{d}V_i}{\frac{1}{2}c\varepsilon_0 P^2 E_0 \cdot E_0^*} \tag{2}$$

where V_i ($i = 1, 2$) is the volume of either the wall or the VSRR, P the unit period, and E_0 the electric field of incident light. Substituting Equation (1) into Equation (2), the calculated results for two subunits are shown in Figure 3b (down panel). At quasi-BICs with strong resonance depth, the wall subunit absorption (A_1) plays a dominant role whereas at off-resonance regions (at/near

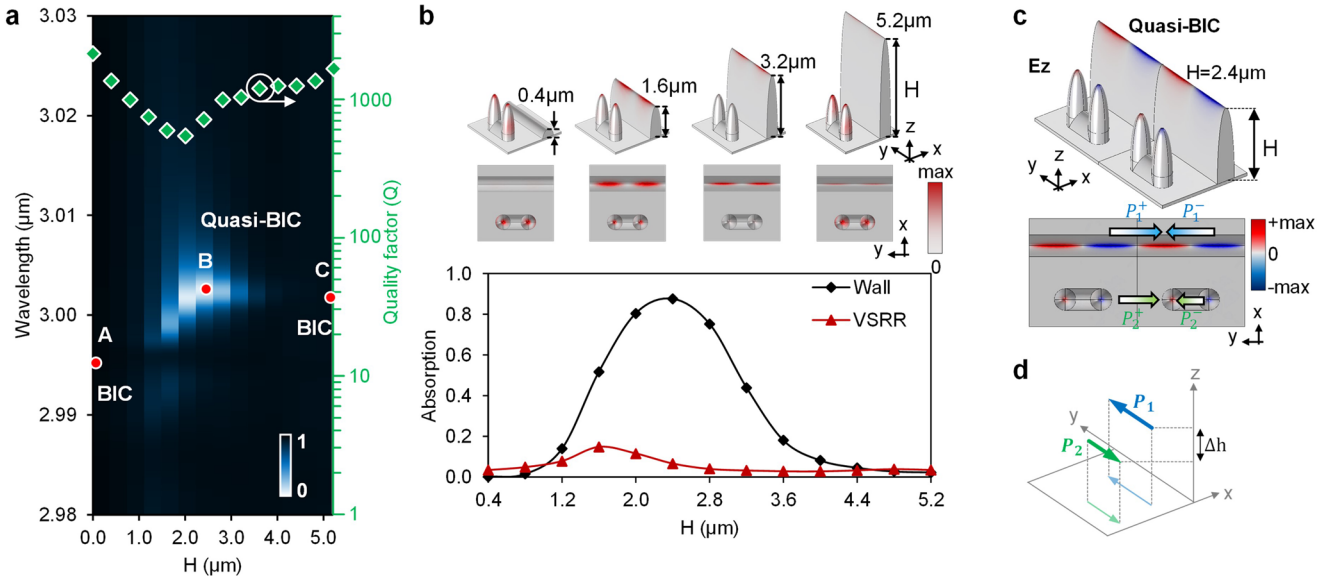

Figure 3. a) Reflection spectra for our metasurfaces with different *H*-parameter (wall height) under *y*-polarized light illumination, whereas other parameters remain unchanged. The green diamond dots represent the corresponding *Q*-factors for various H. The red circular dots mark the positions of 2 BICs and 1 quasi-BIC. b) Top panel: the dissipation power density in metasurfaces units with various wall heights (*H*). Down panel: the absorption respectively induced by the wall and the VSRR at the resonance wavelengths of quasi-BICs for different *H*-parameter. c) The electric field distributions (E_z) at the resonance wavelength for $H = 2.4$ μm (corresponding to point B in (a)). d) The corresponding schematic of net electric dipole moment distribution.

BICs), energy consumption is mainly resulting from the VSRR subunit (A_2).

Recent studies suggested that the resonance amplitude of resonators is equally important as the *Q*-factor in applications related to biosensing.[46] Thus, we choose $H = 2.4$ μm for our metasurface, where both the *Q*-factor (≈715) and the overall absorption amplitude (>0.95) of the quasi-BIC resonance are favorable. The corresponding electric field distribution of the metasurface is shown in Figure 3c. This quasi-BIC resonance can be viewed as a pair of antiparallel dipole moments $P_i = P_i^+ + P_i^-$ (i = 1, 2) with a small distance in the *z*-direction, as shown in Figure 3d. The out-of-plane radiative channel of the quasi-BIC resonance is primarily attributed to two aspects. The first one is the unequalness of magnitude in the two net dipoles ($|P_1| \neq |P_2|$), which will cause dipolar emissions in the far-field.[12] The second aspect is related to the small distance between these two dipoles in the *z*-direction, which would create radiative quadruple components.[47]

3. Circular Dichroism and Quasi-BICs

Having generated sharp quasi-BIC resonance, we then move on to the discussion of circular dichroism. For chiral structures, optical chirality relies on the coupling between the electric field and magnetic field, which obey the constitutive relations[48]

$$\bar{D} = \varepsilon_0 \bar{\bar{\varepsilon}} \bar{E} + \frac{i}{c} \bar{\bar{\xi}} \bar{H}, \quad \bar{B} = \frac{i}{c} \bar{\bar{\zeta}} \bar{E} + \mu_0 \bar{\bar{\mu}} \bar{H} \tag{3}$$

where $\bar{\bar{\varepsilon}}$, $\bar{\bar{\mu}}$, $\bar{\bar{\xi}}$, and $\bar{\bar{\zeta}}$ are 2×2 complex-valued matrices that respectively describe the permittivity, permeability, and the couplings between electric (magnetic) and magnetic (electric) fields. In passive systems with reciprocal responses, the relation between two coupling coefficients can be expressed as $\bar{\bar{\xi}} = -\bar{\bar{\zeta}}^T$, where *T* is the matrix transpose operator. Mathematically, creating sufficient optical chirality requires an increase in the coupling coefficient $\bar{\bar{\xi}}$ to break the degeneracy of left-handed and right-handed circular polarization states (LCP and RCP). Physically and specifically, in metasurface design, the simultaneous breaking of mirror symmetry in 3D space (in-plane and out-of-plane directions) allows for effective coupling between electric and magnetic modes, leading to giant chiral responses.[30,33,38]

In our case, although the out-of-plane mirror symmetry is broken by the asymmetric IRU with two low and height subunits and the golden ground plane, the IRU with parallel VSRR and wall has in-plane mirror symmetry, and thus it cannot support any chirality response (Figure 3c,d). To generate optical chirality, a simple way is to twist the VSRR at an angle with respect to the wall.

An important reason why we choose two dissimilar subunits is to create relatively independent control on the *Q*-factor and the circular dichroism. Importantly, the dissipation energy in the IRU metasurfaces is mainly localized in the wall rather than the VSRR (Figure 3b, down panel), such that $|P_1^{\pm}| \gg |P_2^{\pm}|$ (Figure 3c). Thus, a rotation on the VSRR subunit will not significantly affect the *Q*-factor and resonance amplitude, but it has a giant impact on circular dichroism since the VSRR rotation simultaneously breaks the in-plane and out-of-plane mirror symmetry of the IRU.

To illustrate this, we plot the optical chirality response of an IRU metasurface with a twisted angle of $\theta = 35°$ for the VSRR in **Figure 4**a. Here the left-handed and right-handed circular

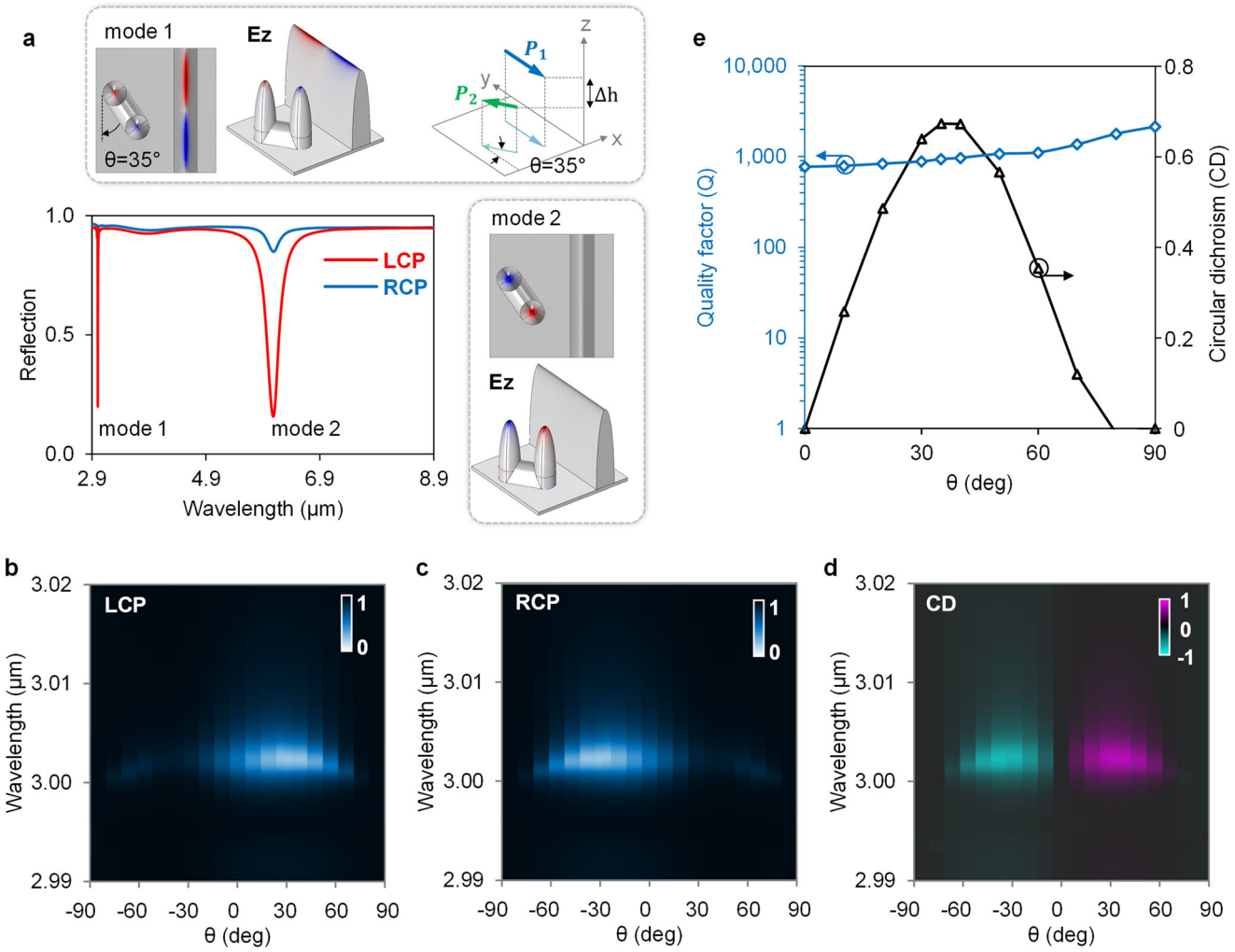

Figure 4. a) Reflection spectra for the proposed metasurfaces with a twisted angle of $\theta = 35°$ for the VSRR under two different circular polarization illuminations. Also shown are the *E*-field distributions for two modes at the resonance wavelengths (LCP), and the corresponding dipolar moments for two subunits. b,c) Reflection spectra for the proposed metasurfaces versus different twisted angles θ for LCP and RCP. d) The corresponding CD signals. e) The dependence of *Q*-factor and circular dichroism (CD) on the asymmetric parameter θ.

polarization states correspond to waves propagating in the negative *z*-direction with polarization unit vectors of $e_{\pm} = e_{\hat{x}} \pm e_{\hat{y}}$. In particular, the chiral metasurface supports two chiral quasi-BIC resonances, which exhibit distinguished different properties. For example, the *Q*-factor of "mode 1" ($Q \approx 938.2$) is more than an order of magnitude higher than that of "mode 2" ($Q \approx 28$).

"Mode 2" is dominated by an in-plane dipolar resonance with strong radiation loss. Also, it strongly squeezes light energy into an ultrasmall volume at the interface between gold and air at/near the tips of VSRR due to its localized nature. This causes strong dissipation loss according to Equations (1) and (2). In sharp contrast, "mode 1" is a nonlocal lattice resonance with BICs origins, whose mode volume is often substantially larger than its localized counterparts and its mode distribution extends largely into the lossless air region rather than being localized at the lossy air–gold interfaces.[49,50] This is an important means to reduce dissipation loss. Also, "mode 1" is a quasi-BIC resonance empowered by the hybridization of both in-plane and out-of-plane multipolar components (Figure 4a top panel), which can desirably suppress the radiation loss. These distinctions in radiation and dissipation loss control explain the *Q*-factor difference between these two modes.

A multipolar analysis of two modes is shown in Figure S1 (Supporting Information) using multipolar decomposition in the Cartesian coordinate, which reveals that the giant CD effects for these two modes result from an efficient interference between the electric modes and the magnetic modes. Also, Our design is robust against geometric parameters perturbation, for both the vertical and horizontal directions (Figure S2, Supporting Information), which is favorable for potential experimental investigation.

Figure 4b,c displays the reflection spectra for IRU metasurfaces with various twisted angles (θ) under LCP and RCP normal incidences, and the corresponding circular dichroism signals are shown in Figure 4d. Here, we define circular dichroism as the reflection difference between the LCP and RCP incidences, such

that CD = $R_{RCP} - R_{LCP}$. Surprisingly, a change in the twisted angle only leads to the modification of the amplitude of CD signals of the quasi-BIC resonances whereas the resonance wavelengths and *Q*-factors stay stable (Figure 4d,e). The CD signal reaches its maximum when $\theta = 35°$ (CD ≈ 0.67), and the corresponding *Q*-factor for the chiral quasi-BIC resonance is $Q \approx 938.2$ with a large resonance depth (>80%) for LCP. This suggests a powerful way for independent control over the *Q*-factor and CD signals of chiral quasi-BIC resonances, where the *Q*-factor is mainly impacted by the height of the wall while the CD is dominated by the twisted angle of the VSRR. Our results are in sharp contrast to previous studies, which face fundamental challenges in the negative correlation between CD signals and the *Q*-factors.[33,35,38]

Importantly, it has been suggested that the dissipation loss in plasmonic systems is crucial for the generation of CD signals, without which the optical chirality must vanish.[51,52] This holds in our plasmonic BIC metasurface. To quantitatively study the influence of metal dissipation loss on the optical chirality of the proposed metasurface, we change the dissipation loss of gold by variating the imaginary part of its permittivity and calculate the corresponding chiral responses, as shown in Figure S3 in the Supporting Information. As the dissipation loss reduces, the *Q*-factor of the chiral quasi-BIC resonances substantially increases while the resonance depth drops dramatically. When the dissipation loss approaches zero, the spectral linewidth of the quasi-BIC resonance gradually disappears, consistent with previous studies.[51,52] This also reveals the BIC roots of the proposed metasurface in dissipation loss control.

Although this is a theoretical work and we change the dissipation loss of gold in our model by simply variating the imaginary part of its permittivity, recent advances in experimental physics reveal several practical ways to reduce optical loss of gold in plasmonic arrays supporting surface lattice resonances. Those experimental methods include the chemical synthesis of monocrystal gold,[53] the use of template stripping fabrication technique,[54] and the thermal annealing process,[55] which can ensure ultrasmooth surfaces for gold nanostructures, from < 1 nm surface roughness to atomical flatness (≈0.2 nm). This help to substantially reduce scattering loss induced by surface roughness and crystal grain boundaries. Also, it has been suggested that changing the incident angle of light can reduce the dissipation loss of gold particle arrays, which is enabled by a transition from a stationary mode (local) to a propagating mode (nonlocal) that is coupled to the Rayleigh anomaly.[49] These experimental methods may shed light on the experimental investigation of the relationship between circular dichroism and the dissipation loss of gold metasurfaces.

4. Conclusions

To summarize, we have successfully resolved the fundamental challenge of incompatibility of high circular dichroism signals and the high *Q*-factors in chiral quasi-BIC resonances. Specifically, by bridging the asymmetric integrated-resonance unit and the BIC physics, we reveal new ways of creating sharp chiral quasi-BICs with independent control of the *Q*-factor and the circular dichroism. Our scheme includes two straightforward steps: (1) the creation of sharp quasi-BIC resonance using metasurfaces with integrated-resonance units; and (2) the generation of chiral quasi-BICs by twisting the vertical split-ring resonator subunit. Importantly, our chiral quasi-BICs are enabled by nonlocal surface lattice resonances, where the modes spatially extend into many adjacent meta-atoms. This nonlocal spatial extend feature is beneficial for applications of chiral drug analysis, biosensing, and quantum entanglement between remote emitters.[56]

5. Experimental Section

Simulations: COMSOL Multiphysics was used for the simulations. In the full-wave simulation, perfect matching layer (PML) conditions were applied along the *z*-direction whereas the periodic boundary conditions were applied in both *x*- and *y*-directions to replicate an infinite array. An input port with $e_{\hat{x}} \pm e_{\hat{y}}$ was used for LCP and RCP normal incidences in the full-wave simulations. Considering that the lattice quasi-BIC mode in the study greatly extends its light field into the air region, the input port was set 30 μm away from the metal ground plane (10 times the operation wavelength), which can avoid undue absorption from the PML layer. The normalized reflection was calculated using

$$R = \frac{\iint Po_z dS + \frac{1}{2} c\varepsilon_0 |E_0|^2 P^2}{\frac{1}{2} c\varepsilon_0 |E_0|^2 P^2} \tag{4}$$

where *S* is a *xy*-plane near the input port, and $Po_z = \frac{1}{2} Re(Ex \cdot Hy^* - Ey \cdot Hx^*)$ is the z-component of the Poynting vector. The permittivity of gold is calculated using the Drude model[57] $\varepsilon = 1 - \omega_p^2/(\omega^2 + i\gamma\omega)$ with the plasma frequency $\omega_p = 1.32 \times 10^{16} s^{-1}$ and the collision frequency $\gamma = 1.2 \times 10^{14} s^{-1}$. The refraction indices of the silica substrate and the photoresist are set as $n = 1.46$.

Supporting Information

Supporting Information is available from the Wiley Online Library or from the author.

Acknowledgements

Y.L. and Y.T. contributed equally to this work. Y.L. and D.P.T. developed ideas. Y.L., J.Y., and Y.T. ran simulations. Y.L., Z.W., S.L., and D.P.T. performed theoretical studies. S.L., Z.W., C.Y., X.G.H., M.K.C, and J.Z. engaged in the result discussion. Y.L., X.G.H., C.Y., and D.P.T. provided supervision. Y.L. and Z.W. wrote the manuscript with contributions from all authors. Support is acknowledged from the Beijing-Hong Kong Universities Alliance (BHUA) fund, the Germany/Hong Kong Joint Research Scheme 2022/23 (NO. 9053045), the University Grants Committee / Research Grants Council of the Hong Kong Special Administrative Region, China (Project No. AoE/P-502/20 and GRF Project: 15303521 and 11310522), National Natural Science Foundation of China (No. 12104296), the Shenzhen Science and Technology Innovation Commission Grant (No. SGDX2019081623281169), the Department of Science and Technology of Guangdong Province (2020B1515120073), and City University of Hong Kong (Project No. 9380131).

Conflict of Interest

The authors declare no conflict of interest.

Data Availability Statement

The data that support the findings of this study are available on request from the corresponding author. The data are not publicly available due to privacy or ethical restrictions.

Keywords

bound states in the continuum, circular dichroism, high-Q resonances, nonlocality, plasmonic metasurfaces

Received: August 6, 2022
Revised: November 3, 2022
Published online:

[1] J. Neumann, E. Wigner, *Zeitschrift* **1929**, *30*, 467470.
[2] C. W. Hsu, B. Zhen, A. Stone, J. Joannopoulos, M. Soljačić, *Nat. Rev. Mater.* **2016**, *1*, 16048.
[3] K. Koshelev, G. Favraud, A. Bogdanov, Kivshar, Y. A. F., *Nanophotonics* **2019**, *8*, 725.
[4] M. Rybin, K. Koshelev, Z. Sadrieva, K. Samusev, A. Bogdanov, M. Limonov, Y. Kivshar, *Phys. Rev. Lett.* **2017**, *119*, 243901.
[5] C. W. Hsu, B. Zhen, J. Lee, S. Chua, S. G. Johnson, J. D. Joannopoulos, M. Soljačić, *Nature* **2013**, *499*, 188.
[6] Z. Deng, F. Li, H. Li, X. Li, A. Alù, *Laser Photonics Rev.* **2022**, *16*, 2100617.
[7] V. Ardizzone, F. Riminucci, S. Zanotti, A. Gianfrate, M. Efthymiou-Tsironi, D. G. Suàrez-Forero, F. Todisco, M. De Giorgi, D. Trypogeorgos, G. Gigli, *Nature* **2022**, *605*, 447.
[8] T. K. Hakala, A. J. Moilanen, A. I. Väkeväinen, R. Guo, J. Martikainen, K. Daskalakis, H. T. Rekola, A. Julku, P. Törmä, *Nat. Phys.* **2018**, *14*, 739.
[9] J. Yang, Z. Huang, D. Maksimov, P. Pankin, I. Timofeev, K. Hong, H. Li, J. Chen, C. Hsu, Y. Liu, *Laser Photonics Rev.* **2021**, *15*, 2100118.
[10] C. Huang, C. Zhang, S. Xiao, Y. Wang, Y. Fan, Y. Liu, N. Zhang, G. Qu, H. Ji, J. Han, Y. Kivshar, Q. Song, *Science* **2020**, *367*, 1018.
[11] A. Leitis, A. Tittl, M. Liu, B. H. Lee, M. B. Gu, Y. S. Kivshar, H. Altug, *Sci. Adv.* **2019**, *5*, eaaw2871.
[12] N. Bernhardt, K. Koshelev, S. White, K. Meng, J. E. Fröch, S. Kim, T. T. Tran, D. Choi, Y. Kivshar, A. Solntsev, *Nano Lett.* **2020**, *20*, 5309.
[13] C. Fang, Q. Yang, Q. Yuan, X. Gan, J. Zhao, Y. Shao, Y. Liu, G. Han, Y. Hao, *Opto-Electron. Adv.* **2021**, *4*, 06200030.
[14] G. Hu, X. Hong, K. Wang, J. Wu, H. Xu, W. Zhao, W. Liu, S. Zhang, F. Garcia-Vidal, B. Wang, *Nat. Photonics* **2019**, *13*, 467.
[15] F. Mattioli, G. Mazzeo, G. Longhi, S. Abbate, G. Pellegrini, E. Mogni, M. Celebrano, M. Finazzi, L. Duò, C. G. Zanchi, *ACS Photonics* **2020**, *7*, 2676.
[16] J. K. Gansel, M. Thiel, M. S. Rill, M. Decker, K. Bade, V. Saile, G. Freymann, S. Linden, M. Wegener, *Science* **2009**, *325*, 1513.
[17] Y. Zhao, M. A. Belkin, A. Alù, *Nat. Commun.* **2012**, *3*, 870.
[18] Z. Wang, H. K. Yao, W. Cai, H. Chen, Y. L. Xiao-Cong, *ACS Photonics* **2016**, *3*, 2096.
[19] Y. Liang, H. Lin, K. Koshelev, F. Zhang, Y. Yang, J. Wu, Y. Kivshar, B. Jia, *Nano Lett.* **2021**, *21*, 1090.
[20] J. Lin, J. Balthasar Mueller, Q. Wang, G. Yuan, N. Antoniou, X. Yuan, F. Capasso, *Science* **2013**, *340*, 331.
[21] Z. Shen, S. Fan, W. Yin, S. Li, Y. Xu, L. Zhang, X. Chen, *Laser Photonics Rev.* **2022**, *16*, 2200370.
[22] C. Zhou, X. Duan, N. Liu, *Nat. Commun.* **2015**, *6*, 8102.
[23] S. Dey, C. Fan, K. V. Gothelf, J. Li, C. Lin, L. Liu, N. Liu, M. Nijenhuis, B. Saccà, F. Simmel, *Nat. Rev. Methods Primers* **2021**, *1*, 13.
[24] Z. Liu, H. Du, J. Li, L. Lu, Z. Li, N. Fang, *Sci. Adv.* **2018**, *4*, eaat4436.
[25] S. Yang, Z. Liu, S. Hu, A. Jin, H. Yang, S. Zhang, J. Li, C. Gu, *Nano Lett.* **2019**, *19*, 3432.
[26] N. Yu, F. Aieta, P. Genevet, M. A. Kats, Z. Gaburro, F. Capasso, *Nano Lett.* **2012**, *12*, 6328.
[27] P. C. Wu, W. Tsai, W. T. Chen, Y. Huang, T. Chen, J. Chen, C. Liao, C. Chu, G. Sun, D. P. Tsai, *Nano Lett.* **2016**, *17*, 445.
[28] E. Plum, X. X. Liu, V. Fedotov, Y. Chen, D. P. Tsai, N. Zheludev, *Phys. Rev. Lett.* **2009**, *102*, 113902.
[29] J. Wu, X. Xu, X. Su, S. Zhao, C. Wu, Y. Sun, Y. Li, F. Wu, Z. Guo, H. Jiang, *Phys. Rev.* **2021**, *16*, 064018.
[30] J. Dixon, M. Lawrence, D. Barton III, J. Dionne, *Phys. Rev. Lett.* **2021**, *126*, 123201.
[31] A. Solntsev, G. S. Agarwal, Y. S. Kivshar, *Nat. Photonics* **2021**, *15*, 327.
[32] Y. Fan, H. Liang, J. Li, D. P. Tsai, S. Zhang, *ACS Photonics* **2022**, *9*, 2872.
[33] M. V. Gorkunov, A. A. Antonov, Y. S. Kivshar, *Phys. Rev. Lett.* **2020**, *125*, 093903.
[34] X. Zhang, Y. Liu, J. Han, Y. Kivshar, Q. Song, *Science* **2022**, *377*, 1215.
[35] T. Shi, Z. Deng, G. Geng, X. Zeng, Y. Zeng, G. Hu, A. Overvig, J. Li, C. Qiu, A. Alù, *Nat. Commun.* **2022**, *13*, 460.
[36] A. Overvig, N. Yu, A. Alù, *Phys. Rev. Lett.* **2021**, *126*, 073001.
[37] Q. Liu, B. Cheng, M. Chao, W. Zhang, Y. Xu, G. Song, *Ann. Phys.* **2021**, *533*, 2100255.
[38] Z. Shen, X. Fang, S. Li, W. Yin, L. Zhang, X. Chen, *Opt. Lett.* **2022**, *47*, 505.
[39] B. Wu, M. Wang, P. Yu, F. Wu, X. Wu, *Opt. Mater.* **2021**, *118*, 111255.
[40] S. Zhao, L. Shao, J. Wang, H. Lin, W. Zhang, *Photonics Res.* **2021**, *9*, 484.
[41] J. Yao, J. Ou, V. Savinov, M. K. Chen, H. Y. Kuo, N. Zheludev, D. P. Tsai, *PhotoniX* **2022**, *3*, 23.
[42] Y. Liang, K. Koshelev, F. Zhang, H. Lin, S. Lin, J. Wu, B. Jia, Y. Kivshar, *Nano Lett.* **2020**, *20*, 6351.
[43] M. Malinauskas, A. Žukauskas, S. Hasegawa, Y. Hayasaki, V. Mizeikis, R. Buividas, S. Juodkazis, *Light: Sci. Appl.* **2016**, *5*, e16133.
[44] C. Menzel, C. Rockstuhl, F. Lederer, *Phys. Rev. A* **2010**, *82*, 053811.
[45] G. Baffou, R. Quidant, C. Girard, *Appl. Phys. Lett.* **2009**, *94*, 153109.
[46] D. Conteduca, G. S. Arruda, I. Barth, Y. Wang, T. F. Krauss, E. R. Martins, *ACS Photonics* **2022**, *9*, 1757.
[47] V. Savinov, V. A. Fedotov, N. Zheludev, *Phys. Rev. B* **2014**, *89*, 205112.
[48] I. Lindell, A. Sihvola, S. Tretyakov, A. Viitanen, *Electromagnetic Waves in Chiral and Bi-Isotropic Media*, Artech House, Boston **1994**.
[49] W. Zhou, Y. Hua, M. D. Huntington, T. W. Odom, *J. Phys. Chem. Lett.* **2012**, *3*, 1381.
[50] Y. Liang, H. Lin, S. R. Lin, J. Y. Wu, W. B. Li, F. Meng, Y. Y. Yang, X. D. Huang, B. H. Jia, Y. Kivshar, *Nano Lett.* **2021**, *21*, 8917.
[51] A. B. Khanikaev, N. Arju, Z. Fan, D. Purtseladze, F. Lu, J. Lee, P. Sarriugarte, M. Schnell, R. Hillenbrand, M. A. Belkin, *Nat. Commun.* **2016**, *7*, 12045.
[52] Y. Zhao, A. Alù, *Phys. Rev. B* **2011**, *84*, 205428.
[53] Y. Lebsir, S. Boroviks, M. Thomaschewski, S. I. Bozhevolnyi, V. A. Zenin, *Nano Lett.* **2022**, *22*, 5759.
[54] Y. Shen, K. He, Q. S. Zou, S. Xing, J. Y. Huang, M. C. Zheng, X. Y. She, C. J. Jin, *Adv. Funct. Mater.* **2022**, *32*, 2108741.
[55] S. Deng, R. Li, J. Park, J. Guan, P. Choo, J. Hu, P. Smeets, T. W. Odom, *Proc. Natl. Acad. Sci. USA* **2020**, *117*, 23380.
[56] A. K. Boddeti, J. Guan, T. Sentz, X. Juarez, W. Newman, C. Cortes, T. W. Odom, Z. Jacob, *Nano Lett.* **2021**, *22*, 22.
[57] G. Dolling, C. Enkrich, M. Wegener, C. M. Soukoulis, S. Linden, *Science* **2006**, *312*, 892.